Lead, zinc, nickel and chromium ions removal from polluted waters using zeolite formed from bauxite, obsidian and their combination with red mud: Behaviour and mechanisms

Claudia Belviso [a,*], Paola Lucini [b], Maura Mancinelli [c], Maryam Abdolrahimi [d,e], Annalisa Martucci [c], Davide Peddis [e,f], Federica Maraschi [b], Francesco Cavalcante [a], Michela Sturini [b]

[a] *Istituto di Metodologie per l'Analisi Ambientale – IMAA-CNR, 85050, Tito Scalo, PZ, Italy*
[b] *Department of Chemistry, University of Pavia, 27100, Pavia, Italy*
[c] *Department of Physics and Earth Sciences, University of Ferrara, 44122, Ferrara, Italy*
[d] *Dipartimento di Scienze, Università degli Studi Roma Tre, 00146, Roma, Italy*
[e] *Istituto di Struttura della Materia, ISM-CNR, 00015, Monterotondo Scalo, RM, Italy*
[f] *Dipartimento di Chimica e Chimica Industriale, Università di Genova, I-16146, Genova, Italy*

ARTICLE INFO

ABSTRACT

Synthetic zeolites obtained combining natural sources (bauxite and obsidian), pure alumina/silica reagents, and waste material (red mud) were tested for heavy metals (i.e., Pb^{2+}, Zn^{2+}, Ni^{2+}, Cr^{3+}) removal. The adsorption capabilities of the formed sodalite, zeolite A and zeolite X (LTA and FAU topology, respectively), were compared through thermodynamic and kinetic experiments. Although all the newly-formed zeolites were able to remove the pollutant elements within 24 h, Zeolite X and sodalite synthesized combining obsidian (natural material as silica source) and red mud (waste material as alumina source) proved to be a better sorbent phase (q_{max} 20–25 mg g^{-1}) compared to Zeolite A formed from treated bauxite (q_{max} 4–18 mg g^{-1}). Their removal efficiency was also evaluated in polluted waters (wastewater treatment plant [WWTP] effluent, heavy metals mixture, native pH). Depending on synthesized zeolite type, the adsorption mechanism was accredited to ion exchange and precipitation mechanisms. The location of metal-ions inside the zeolite channels was defined by X-ray Powder Diffraction (XRPD) Rietveld analysis. Host–guest interactions among the framework oxygen atoms, co-adsorbed water molecules, and metal-ions were highlighted by the refined bond distances. Finally, magnetic characterization allowed the recognize of different magnetic properties as a function of raw materials used for zeolite synthesis.

1. Introduction

Water pollution is an increasing problem in most countries worldwide, and heavy metals remediation is one of the major concerns. Several strategies have been proposed to reduce the level of water pollutants (Sun et al., 2003; Fu et al., 2020; Jinendra et al., 2019a, 2019b; Jyothi et al., 2019), including more eco-friendly methods based on the use of natural sorbents as alternative and green extractive materials, such as biomaterials (Srivastava et al., 2015; Senthil Kumar et al., 2018; Kiruba et al., 2014; Inyang et al., 2016; Saravanan et al., 2020) or clays (Yin et al., 2020; Ozdes et al., 2011; Vhahangwele and Mugera, 2015;

Sen and Gomez, 2011; He et al., 2011; Jiang et al., 2010).

Among minerals, zeolites have been widely used to solve environmental problems due to their peculiar structural features. Zeolites are microporous materials whose structure is characterized by a framework of linked tetrahedra consisting of four oxygen atoms surrounding a cation. The structure contains cages and channels occupied by H_2O molecules or extra-framework cations commonly exchangeable (Coombs et al., 1997).

The attention has widely focused on the application of natural/ modified zeolites for heavy metals removal from wastewater (e.g., Mancinelli et al., 2020; Sprynskyy et al., 2006; Fu et al., 2020; Liu et al.,

---

2014; Abatal et al., 2018; Salman et al., 2017; Kareem and Dawagreh, 2017), although many synthetic equivalents exhibit similar or higher properties (Kuang et al., 2015; Kozara-Sucharda et al., 2020; Ren et al., 2022). Other synthetic zeolites have been produced at lower cost from waste materials as cheaper sources of silica and/or alumina (Alberti et al., 2019; Psycharis et al., 2004; Ng et al., 2015; Belviso et al., 2015, 2016, 2018; Yoldi et al., 2019; Kuroki et al., 2019; Gao et al., 2019), and have successfully used for heavy metals remediation (e.g., Shawabkeh et al., 2004; Belviso et al., 2014, 2021; Abdelrahman et al., 2021; Hussain et al., 2021; Zhang et al., 2021; Chuenpratoom et al., 2021). Also zeolite formed from clays or other zeolites have been extensively documented (Gualtieri et al., 1997; Mezni et al., 2011; Wruck et al., 2021, He et al., 2021). On the contrary, very few data displayed the successful use of other natural sources, such as obsidian and bauxite, for zeolite synthesis (Belviso, 2016; Belviso et al., 2020a, 2022; Wang et al., 2013; Motoharu and Katsutoshi, 1997) and, to our knowledge, the efficiency of the as-prepared zeolites, alone or in combination with waste materials in heavy metals removal from waters has not yet been investigated.

In this paper, obsidian, bauxite and red mud were used as silica, alumina and magnetic nanoparticle sources to form zeolites. Red mud, a waste produced by the caustic leaching process to extract aluminium from bauxite, was chosen for its alumina content and the high amount of iron oxy-hydroxides which induces interesting magnetic behaviour in synthetic zeolites (Belviso et al., 2015, 2018; Cheng et al., 2020). The synthetic products were tested to remove heavy metals from polluted water and the mechanism controlling the remediation process was identified for each type of zeolite formed.

These experiments aim to broaden the typology of sources to be used to synthesize very useful minerals such as zeolites. In addition, they move an innovative double step forward in the circular economy proposing a circular water management model by synthetic minerals from waste thus no longer considered as material to be deposited in landfill but as a valuable resource to be transformed into products capable of guaranteeing the protection of an equally precious and limited resource such as water.

2. Materials and methods

Sodium silicate, sodium aluminate, and sodium hydroxide were purchased from Aldrich Chemicals Ltd. $Pb(NO_3)_2$, $ZnSO_4 \cdot 7H_2O$, $NiSO_4 \cdot 7H_2O$, and $CrCl_3 \cdot 6H_2O$ were purchased from Carlo Erba reagents (Milano, Italy). Chemical purity was assured to be >98%.

Natural bauxite (BA) collected from Upper Cretaceous bauxites (southern Italy); rhyolitic obsidian (OS) from Lipari, Aeolian Island (Italy), and red mud (RM) coming from aluminium extraction area close to Podgorica (Montenegro) were used as raw material for the zeolite synthesis. Chemical composition (major elements) of these raw materials was determined by X-ray fluorescence (XRF) (Philips PW 1480). The mineralogy was analyzed by X-ray diffraction (XRD) using a Rigaku Rint 2200 powder diffractometer equipped with Cu-Kα radiation and a graphite monochromator.

Tap water was collected from the Pavia municipal waterworks. The effluent sample was from an urban wastewater treatment plant (WWTP) in an industrialized and agricultural area of the Lombardy plan (Vigevano, PV).

2.1. Synthesis process

A hydrothermal process at low temperature was used to form zeolite starting from the four unconventional sources described above.

2.1.1. Synthesis from bauxite (BA_Hy60)

Pre-fused NaOH bauxite (1.2:1 wt ratio at 600 °C for 1 h in a muffle furnace) was mixed with distilled water and kept in stirring for a night. After that, the mixture was incubated in a water bath for 4 days at 60 °C.

Finally, the solid was separated by centrifugation, rinsed three times with distilled water, and dried in the oven for 12 h at 80 °C.

2.1.2. Synthesis from obsidian (OS_Hy60)

4.00 g of obsidian and 4.80 g of NaOH were ground in a mechanical mortar for 2 min and then heated in a muffle furnace at 550 °C for 1 h. The solid mass was crushed, mixed with distilled water, stirred for 1 night, and submitted to aging for 4 days by a hydrothermal process at 60 °C (Belviso, 2016; Belviso et al., 2020a).

2.1.3. Synthesis from obsidian and red mud (OSRM_Hy60)

A mixture of obsidian and red mud (50:50) was pre-fused with NaOH bauxite at 600 °C for 1 h in a muffle furnace and submitted at the same steps described above before the hydrothermal process for 4 days in a water bath at 60 °C.

2.1.4. Synthesis from pure silica/alumina source and red mud (PSA_Hy60)

The zeolite synthesis was carried out using sodium aluminate and silicate as described in our previous paper (Belviso et al., 2020b). RM was previously pre-fused at 600 °C with NaOH and aged using an ultrasonic water bath to form layered double hydroxide composite material.

2.1.5. Scanning electron microscopy (SEM)

The morphological features of all the synthetic zeolites were carried out using a field emission scanning electron microscope (SEM, Zeiss Supra 40) combined with energy-dispersive X-ray spectrometer (EDS, Oxford Inca Energy 350) equipped with a Si(Li) detector. To avoid charging of the surface, the samples were carbon-sputtered (10 nm thick).

2.2. Fourier-transform infrared spectroscopy (FTIR)

Synthetic product before and after heavy metals adsorption process were investigated by Fourier-transform infrared spectroscopy (FTIR). FT-IR spectra were obtained with a Cary 630 FTIR spectrometer (Agilent, Cernusco sul Naviglio, Italy) equipped with Diamond ATR (attenuated total reflectance) sampling module (range 4000–650 cm^{-1}, resolution 4 cm^{-1}).

2.3. X-ray powder diffraction

XRD data were collected at room temperature on a Bruker D8 Advance Da Vinci diffractometer (Bruker AXS, Germany, CuKα radiation and a Ni filter) working in Bragg-Brentano geometry and equipped with a LynxEye XE silicon strip detector (angular range of the detector window size = 2.585° 2θ) set to discriminate Cu Kα$_{1,2}$ radiation. The measurements were performed in 2θ range of 3–110 °2Θ, angular step size of 0.02°2Θ and scan-step time of 12 s. Qualitative phase analysis of collected patterns was performed by means of the Bruker AXS EVA software (v.5) and refined by means of the fundamental-parameter approach (TOPAS v.5.0). The structural refinements were run through a full profile Rietveld analysis using the GSAS software (Larson and Von Dreele, 2000) and the EXPGUI graphical interface (Toby, 2001). Modal Quantitative Phase Analysis (QPA) was also performed using Rietveld refinement combined with the internal standard method to provide an estimate of both the crystalline and the amorphous phase as a mixture. The powders samples were mixed with 10 wt % Corundum NIST SRM 676 and accurately ground again to homogenize the mixture. For the polycrystalline mixtures, the weight fractions of all phases of the mixtures including the internal standard were refined by the Rietveld method. The unit cell parameters were refined together with the background (a Chebyshev polynomial with twelve-terms) and the Finger, Cox and Jephcoat profile pseudo-Voigt profile function (Finger et al., 1994). The location of extra-framework species was carried out by the Analysis of difference Fourier map. Positional parameters, occupancy

factors, and displacement parameters are reported in Table S1, framework atom distances and angles in Table S2, and coordination of extra-framework cations in Table S3. The refinement also included a 2θ-zero shift and a scale factor. All structure drawings were produced by the VESTA program (Momma and Izumi, 2011).

CrystalMaker program (version 8.6.2) was used to calculate the percentage of free space (i.e., the space not filled by atom spheres) in zeolites before and after metal adsorption. For the two latter calculations, van der Waals radii were used.

2.4. Thermal analyses

Thermogravimetric (TG) and differential Thermal Analysis (DTA) curves were obtained through the Netzsch STA 409 PC LUXX® (Gerätebau, Germany) simultaneous TG/DTA thermogravimetric balance. Thermal analyses were performed from 20 °C to 1000 °C, with a heating rate of 5 °C min^{-1} under air flow (flow rate 20 mL min^{-1}).

2.5. Magnetization measurements

DC magnetization measurements were investigated using a vibrating sample magnetometer (VSM Model 10 – Microsense) equipped with an electromagnet producing magnetic field in the range from −2 to +2T. Each sample, in the form of powder, was fixed in a capsule using epoxy resin to prevent any movement of the nanoparticles during the measurements.

2.6. Adsorption and kinetic experiments

Experiments were performed using Pb^{2+}, Zn^{2+}, Ni^{2+}, and Cr^{3+} stock solutions (concentration range between 420 and 920 mg L^{-1}) prepared from $Pb(NO_3)_2$, $ZnSO_4 \cdot 7H_2O$, $NiSO_4 \cdot 7H_2O$, and $CrCl_3 \cdot 6H_2O$ in distilled water.

Metal-ions measurements were carried out by inductively coupled plasma optical emission spectroscopy (ICP-OES iCAP 7400, Thermo Fischer Scientific) equipped with a concentric nebulizer, cyclonic spray chamber, and ceramic duo-torch, according to the operating conditions suggested by the manufacturer. The quantification was obtained by external calibration (standards from 1 to 50 mg L^{-1} in 0.5% v/v ultrapure HNO$_3$). An optimal linearity (R$^2 \geq 0.999$) was reached for all the analytes.

For the equilibrium experiments, a fixed amount of each zeolite (20 mg) was suspended in 10 mL of NaNO$_3$ 0.01 M solutions spiked with increasing amounts of metals (from 5 to 100 mg L^{-1}), each separately, at room temperature. Flasks were gently shaken overnight by a roller shaker. After equilibration, the suspensions were centrifuged, and the supernatants were filtered (0.45 μm nylon syringe filter), acidified with 0.5% v/v ultrapure HNO$_3$, and analyzed by ICP-OES to determine metal-ions concentration at equilibrium (C_e). Isotherm curves were obtained plotting the adsorbed metal-ions amount at equilibrium (q_e, mg g^{-1}) calculated by Eq. (1) *vs* the residual metal-ions concentration in solution after equilibration (C_e, mg L^{-1}):

$$q_e = \frac{(C_0 - C_e) \cdot V}{m} \tag{1}$$

where C_0 is the concentration of the initial metal-ions (mg L^{-1}), V is the volume of the solution (L), and m is the amount of the sorbent material (g).

For the kinetic tests, flasks containing 10 mL of a fixed metals concentration (60 mg L^{-1} Pb^{2+}, 55 mg L^{-1} Zn^{2+}, 50 mg L^{-1} Ni^{2+}, 40 mg L^{-1} Cr^{3+}), each separately, were contacted with a constant amount of zeolite (20 mg) and shaken by a roller shaker, at room temperature. At the planned time, the supernatant (100–500 μL) was collected, diluted (3 mL), filtered (0.45 μm nylon syringe filter), acidified with 0.5% v/v ultrapure HNO$_3$, and analyzed by ICP-OES. The kinetic profiles were

obtained plotting the adsorbed metal-ions amount at time t (q_t, mg g^{-1}) calculated from Eq. (2) *vs* time (t, min):

$$q_t = \frac{(C_0 - C_t) \cdot V}{m} \tag{2}$$

where C_0 is the initial metal-ions concentration (mg L^{-1}), C_t the metal-ions concentration in solution at time t (mg L^{-1}), V the volume of the solution (L), and m the amount of the sorbent material (g).

All the experimental data were performed in duplicated, and the thermodynamic and kinetic parameters were estimated by dedicated software (OriginPro, Version, 2019b. OriginLab Corporation, Northampton, MA, USA).

2.7. Heavy metals removal from actual matrices

Tap water and WWTP effluent samples were spiked with two metal-ions concentrations (3–6 and 50–87 mg L^{-1}). 20 mg of each sorbent material was suspended in 10 mL of the spiked water sample and shaken for 24 h. Then some mL of the supernatants were withdrawn, filtered, acidified, and analyzed by ICP-OES. The adsorption efficiencies (*Ads%*) were determined by Eq. (3):

$$Ads\% = \frac{C_0 - C_e}{C_0} \cdot 100 \tag{3}$$

3. Results and discussion

3.1. Raw materials

The chemical and mineralogical compositions of raw materials are shown in Table 1 and Fig. 1, respectively. The results indicate that BA is characterized by the typical composition of bauxite, showing the presence of a high percentage of Al$_2$O$_3$ (41.41%) and Fe$_2$O$_3$ 15.22%; SiO$_2$ is estimated equal to 25.95% (Table 1). These values are consistent with the mineralogy represented by kaolinite, boehmite, goethite, hematite and anatase (Fig. 1a). OS chemical composition shows a high percentage of SiO$_2$ (74.2%) (Table 1), indicative of a large amount of amorphous glass material also confirmed by the broad band determined on the X-ray pattern (Fig. 1b). Finally, Table 1 displays that SiO$_2$ and Al$_2$O$_3$ percentages in RM are 7.89% and 11.46%, respectively; Fe$_2$O$_3$ is high and equal 36.8%. XRDP profile of this waste material shows the presence of hematite/goethite/pyrite and gibbsite with lower amounts of calcite and sodalite (Fig. 1c).

The generally large amount of both silica and alumina in all the samples confirms that the selected raw materials are suitable as sources for zeolite synthesis (Belviso, 2016; Belviso et al., 2018, 2020a, 2022; Choi et al., 2002; Wang et al., 2013). Moreover, the high percentage of iron oxide-hydroxides suggests the possibility of successfully exploiting the chemical composition of all materials to give synthetic products with magnetic properties (Belviso et al., 2018, 2020c; Alberti et al., 2019; Xie et al., 2018). This is confirmed by a detailed raw materials magnetic investigation. Field dependence magnetization of the raw materials at

Table 1
Raw materials chemical composition (wt %).

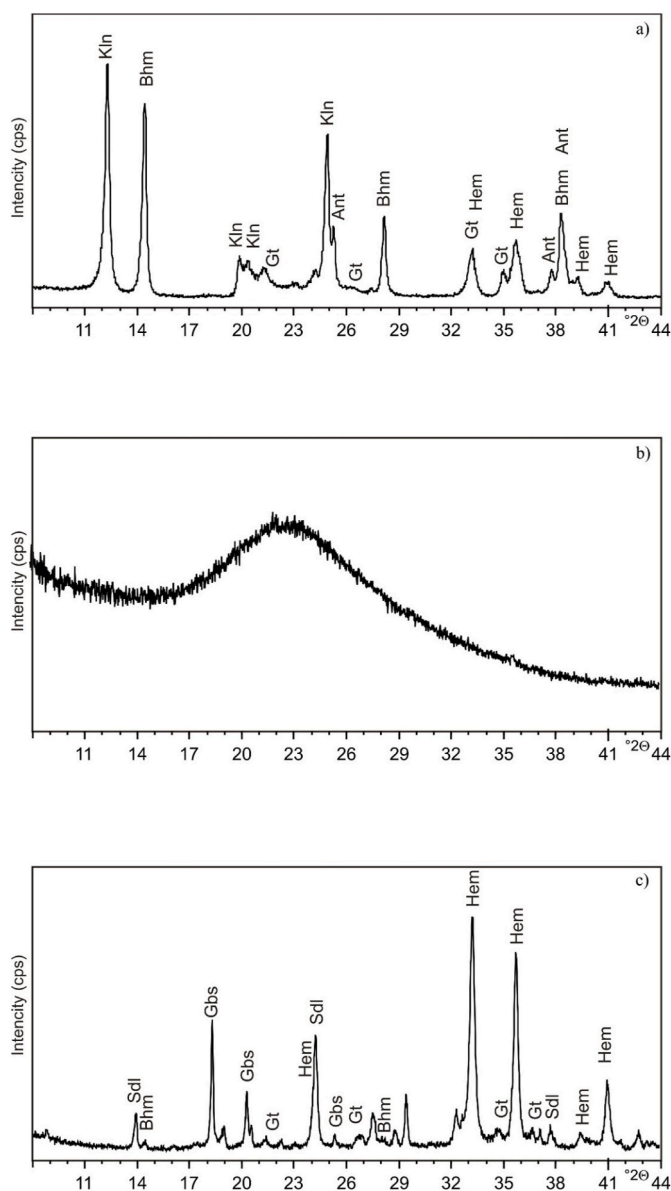|	BA	OS	RM
Na$_2$O	0.05	4.31	4.03
MgO	0.18	0.15	0.21
Al$_2$O$_3$	41.4	13.2	11.5
SiO$_2$	26.0	74.2	7.89
P$_2$O$_5$	0.05	0.02	0.09
K$_2$O	0.14	4.94	0.45
CaO	0.49	0.96	3.53
TiO$_2$	3.71	0.09	4.82
MnO	0.03	0.08	0.21
Fe$_2$O$_3$	15.2	1.76	36.8
SiO$_2$/Al$_2$O$_3$	0.63	5.62	0.69

Fig. 1. XRD patterns of a) bauxite (BA), b) obsidian (OS) and c) red mud (RM) samples. Kln: kaolinite; Bhm: boehmite; Hem: hematite; Gt:goethite; Ant: anatase; Gbs:gibbsite; Sdl:sodalite.

Fig. 2. Field dependence of magnetization recorded at 300 K of a) bauxite (BA), b) obsidian (OS) and c) red mud (RM) samples.

300 K is reported in Fig. 2. All the samples show a hysteretic behaviour (i.e., presence of remanence magnetization and coercive fields). Both BA and RM samples (Fig. 2a and b, respectively) present a linear increase of magnetization in the higher field (typical of an antiferromagnetic behaviour) superimposed to a small ferromagnetic contribution in the lower field region, indicating that the magnetism of these samples is dominated by antiferromagnetic oxy-hydroxides (hematite–goethite) with a small percentage of ferro(ferri)magnetic oxides. The effective magnetic moment (M_{eff}) due to the ferro(ferri)magnetic component has been determined by the extrapolation to zero of the high-field linear portion. The extracted values of M_{eff} are ~0.4 and ~0.3 Am^2kg^{-1} for BA and RM samples, respectively, which is much higher than what is expected for nanostructured hematite (<0.05 Am^2kg^{-1}), suggesting that the ferromagnetic contribution can be ascribed to the presence of ferro (ferri)magnetic oxides phases and not to the uncompensated spin of nanostructured hematite. BA sample (Fig. 2a) shows a wasp-waisted shape at low field that can be ascribed to the partial doping of hematite with aluminium (Murad and Schwertmann, 1986; Jiang et al., 2012,
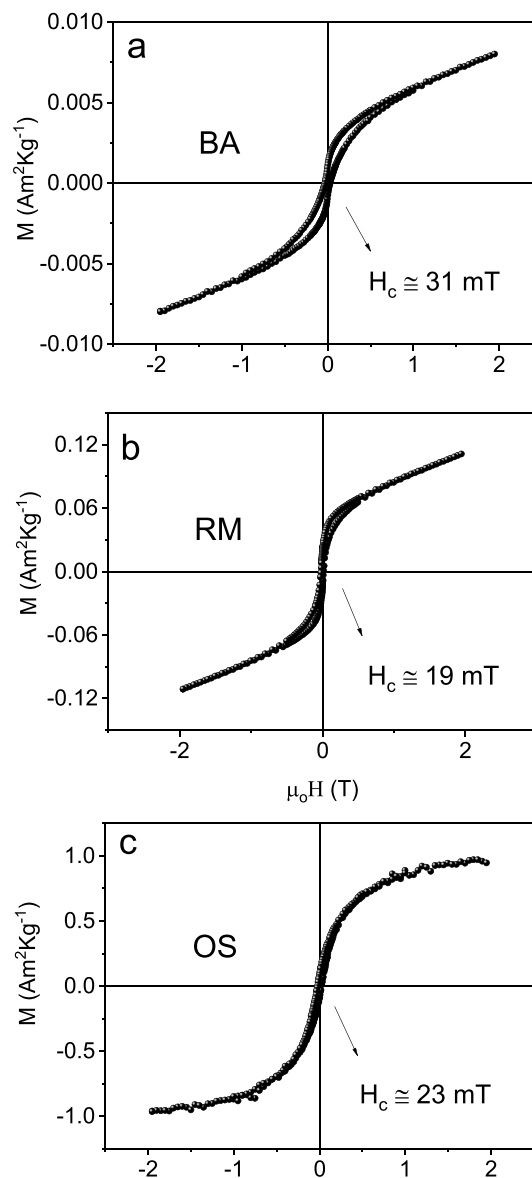
2015). This effect is also evident in the RM sample, even with a much weaker intensity.

The magnetic landscape shown by raw materials is consistent with the mineralogical composition characterized by the presence of oxy-hydroxides (hematite–goethite) with a small percentage of ferro(ferri) magnetic oxides and aluminium oxide with decreasing content going from BA to RM sample (Fig. 1). The field dependence magnetization of OS sample indicates a different behaviour, showing a ferromagnetic-like saturated hysteresis with a low saturation magnetization (Ms $\cong$ 0.96 Am^2kg^{-1}) (Mameli et al., 2016; Belviso et al., 2020a). This indicates that the magnetic behaviour in this sample is dominated by some ferrimagnetic oxides like maghemite (γ-Fe_2O_3) or magnetite (Fe_3O_4), present in relatively low percentages with respect to other non-magnetic or antiferromagnetic compounds.

3.2. Synthetic products characterization

All the investigated samples are polyphasic mixtures except for BA_Hy60 and OS_Hy60. Different percentages of sodalite, zeolite A (LTA-topology), and zeolite X (FAU- topology) characterize the

mineralogical composition of the synthetic products.

SEM images provide information on the habit of the newly-formed zeolites showing the rose-like morphology of sodalite, the typical cubic shape of LTA-type, and the octahedral shape of FAU crystals (Fig. S1).

3.2.1. Analysis by rietveld refinement

Zeolites with FAU-type topology are characterized by sodalite units (β-cage, cubooctahedron) linked together by double 6-rings (d6R, hexagonal prism), thus creating large supercages (referred also as α-cages) delimited by 12-ring apertures (Fig. 3). The three-dimensional LTA framework can build up by β-cage related by pure translations along the cube axes, linked through double 4-rings. The 8-ring channels are parallel to <100>, and their intersections are equal to the α-cavity (Fig. 3).

The amount of the crystalline phases is: 100 wt% of zeolite A in its sodium form for BA_Hy60; 58 wt% of zeolite Na-A, 29 wt% of sodalite, and 13 wt% of hydrotalcite for PSA_Hy60; 100 wt% of zeolite X in its sodium form for OS_Hy60; and 34 wt% of zeolite Na-X and 66 wt% of sodalite for OSRM_Hy60. The crystallinity is ~50 wt% in all samples with respect to the amorphous phase (Table S4).

3.2.2. Structural characterization by X-ray diffraction and thermal analysis

Based on the refined occupancy and symmetry, 121 Na^+ cations (very near to the maximum number theoretically achievable per unit cell) and approximately 287 water molecules are localised in the

a)

b)

Fig. 3. Projection along [111] and [001] of a) FAU- and b) SOD-type frameworks, respectively.

OS_Hy60 zeolite channels (Table 2). On the whole, the structure refinement gives a water content of ~26% in weight, in very good agreement with the weight loss registered (25–1000 °C temperature range) by thermogravimetric analysis (about 23% zeolite dry weight (dw), see Fig. 4). The refined distances of the O atoms in the water molecules from themselves and the framework oxygens suggest the presence of water chains interacting with O1, O2, and O4 framework oxygen atoms (Table S1, Table S2).

In BA_Hy60 (LTA topology, $Pm3m$ space group), difference Fourier map highlights the presence of seven extra framework sites: three of these are occupied by Na^+ cations (Na1, Na2, and Na3 sites), the residual ones by water molecules (W1, W2, W3, and W4 sites) (Table S1). Cations at Na1 and Na2 (located on threefold axis) sites are both coordinated to O2 and O3 framework oxygens, while Na^+ lying on Na3 site is only bonded to water molecules (Table S3). Also in this case, zig-zag water chains are laterally branched to O1 and O3 framework O atoms (Table S1). Overall, ~12 Na ions and 26 water molecules (corresponding to a water content of ~26% in weight in excellent agreement with TG analyses) are detected (Table 3). Using the CrystalMaker Software, the porosity (corrected for first nearest-neighbor sphere overlap and site visibility) of both BA_Hy60 and OS_Hy60 is determined: in BA_Hy60, the filled space is 782.46 $Å^3$ (42.41%) per unit cell, the void space amounts for 1062.60 $Å^3$ (57.59%) per unit cell. In OS_Hy60, the filled space has been calculated to be 6483.46 $Å^3$ (41.98%) per unit cell, and the void space augments to 8962.27 $Å^3$ (58.02%).

In both OS_Hy60 and BA_Hy60 samples, DTA curves highlight a great endothermic signal extending from room temperature up to ~220 °C due to the loss of weakly-bounded water molecules. TG thermograms showed another weight loss in the 250–600 °C range, due to the departure from the structure of structural water trapped in the zeolite microporosities and bound to the extraframework cations. The exothermic peak at high temperature is indicative of the zeolites thermal stability and lattice collapse. This signal is observed in the range 800–870 °C and 800–900 °C for OS_Hy60 and BA_Hy60, respectively, and is ascribable to the breakdown of the zeolite structure with the consequent formation of an amorphous phase.

3.2.3. Magnetic properties

The field dependence of magnetization recorded at 300 K of synthetic products (Fig. 5) shows different magnetic behaviour with respect to the raw materials due to the formation of different zeolites. BA_Hy60 shows nearly perfect antiferromagnetic behaviour that can be ascribed to the presence of hematite crystals precipitated on the surface of zeolites (Belviso et al., 2015). A ferromagnetic contribution at low field becomes progressively more evident in the order BA_Hy60, OSRM_Hy60, and OS_Hy60 (Belviso et al., 2020c).

As already discussed, the high value of M_{eff} observed for OSRM_Hy60 and OS_Hy60 (i.e.,: ~0.2–1 Am^2Kg^{-1}) indicates that the ferromagnetic behaviour can be ascribed to the presence of ferro (ferri)magnetic oxides phases and not to the uncompensated spin of nanostructured hematite (Suber et al., 2010).

The magnetic behaviour drastically changes in the PSA_Hy60 sample showing a ferromagnetic-like behaviour with a very low saturation magnetization (Ms ≅ 0.07 Am^2kg^{-1}). Also in this sample, a clear wasp-waisted shape of hysteresis is observed, ascribed to the presence of hematite doped by aluminium, as shown in BA samples. This indicates that the magnetic behaviour in this sample is dominated by some ferrimagnetic oxides present as a minor percentage in a matrix of antiferromagnetic doped hematite.

3.3. Pb^{2+}, Zn^{2+}, Ni^{2+}, and Cr^{3+} adsorption

3.3.1. Preliminary investigation

Before starting the equilibrium and kinetic experiments, the pH effect on Pb^{2+}, Zn^{2+}, Ni^{2+}, and Cr^{3+} adsorption onto BA_Hy60, PSA_Hy60, OS_Hy60, and OSRM_Hy60 was investigated.
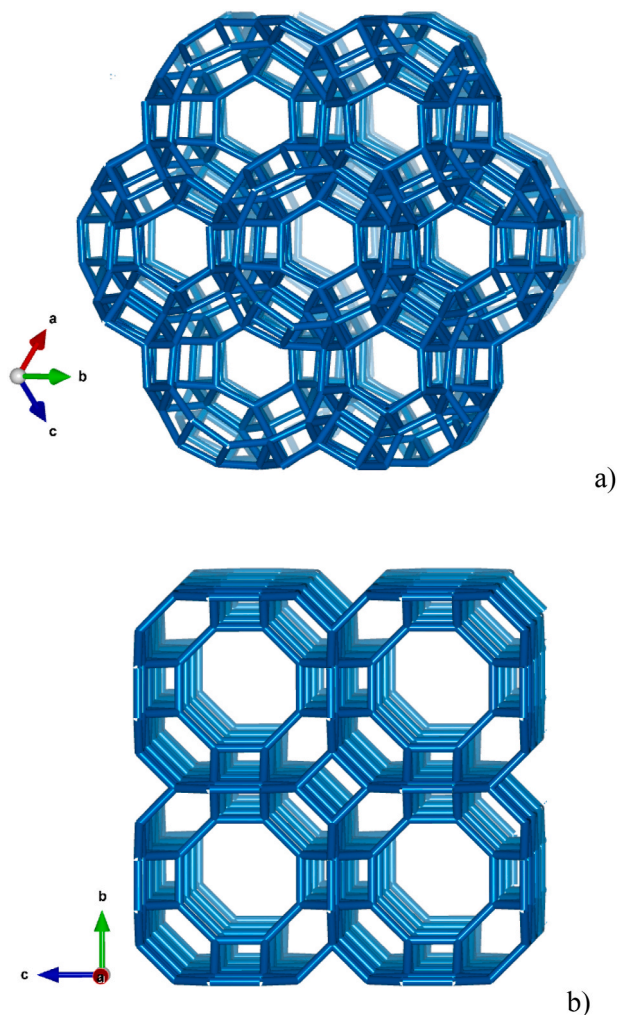
Table 2
Positions of the extra-framework cations in the Ba-HY-60 and OS-HY-60 zeolite as inferred from structure refinement based on the experimental XRD patterns. The atoms per unit cell on a given crystallographic site is given by a number before the symbol of the site.

| Sample	Site name	Site Multiplicity	Site position	Site symmetry	Positional parameters	Atoms per unit cell	Cations Weight %
	Na1	8	x, x, x	3m(111)	0.243, 0.243, 0.243	4.32	
Ba-HY-60	Na2	8	x, x, x	3m(111)	0.154, 0.154, 0.154	5.24	Na 12.7%
	Na3	12	1/2, y, y	mm2(011)	1/2, 0.294, 0.294	2.82	
Ba-HY-Cr	Na1	8	x, x, x	3m(111)	0.244, 0.244, 0.244	5.6	Na 5.8%
	Cr3	12	1/2, y, y	mm2(011)	1/2, 0.380, 0.380	2.20	Cr 5.2%
Ba-HY-Ni	Na1	8	x,x,x	3m(111)	0.244, 0.244, 0.244	8.00	Na 8.5%
	Ni3	12	1/2, y, y	mm2(011)	1/2, 0.433, 0.433	1.37	Ni 3.7%
Ba-HY-Zn	Na1	8	x, x, x	3m(111)	0.236, 0.236, 0.236	2.44	
	Na2	8	x, x, x	3m(111)	0.161, 0.161, 0.161	2.35	Na 4.5%
	Zr3	12	1/2, y, y	mm2(011)	1/2, 0.306, 0.306	3.94	Zn 10.6%
Ba-HY-Pb	Pb1	8	x, x, x	3m(111)	0.248, 0.248, 0.248	1.56	
	Pb2	8	x, x, x	3m(111)	0.159, 0.159, 0.159	1.11	Pb 36.0%
	Pb3	12	1/2, y, y	mm2(011)	1/2, 0.289, 0.289	3.31	
	Na1	32	x, x, x	3(111)	0.720, 0.720, 0.720	16.00	
OS-HY-60	Na2	32	x, x, x	3(111)	0.247, 0.247, 0.247	16.00	Na 14.4%
	Na3	32	x, x, x	3(111)	0.07, 0.07, 0.07	22.40	
	Na4	96	x, y, z	1	0.116, 0.076, 0.540	67.20	
OS-HY-Cr	Cr1	32	x, x, x	3(111)	0.700, 0.700, 0.700	16.03	
	Cr2	32	x, x, x	3(111)	0.221, 0.221, 0.221	13.76	Cr 8.2%
	Na3	32	x, x, x	3(111)	0.07, 0.07, 0.07	9.60	Na 3.8%
	Na4	96	x, y, z	1	0.121, 0.06, 0.567	22.08	
	Ni1	32	x, x, x	3(111)	0.698, 0.698, 0.698	12.45	
OS-HY-Ni	Ni2	32	x, x, x	3(111)	0.234, 0.234, 0.234	6.78	Ni 15.4%
	Na3	32	x, x, x	3(111)	0.07, 0.07, 0.07	7.55	Na 0.8%
	Ni4	96	x, y, z	1	0.118, 0.08, 0.547	33.70	
	Zn1	32	x, x, x	3(111)	0.720, 0.720, 0.720	16.00	
OS-HY-Zn	Zn2	32	x, x, x	3(111)	0.247, 0.247, 0.247	16.00	
	Na3	32	x, x, x	3(111)	0.07, 0.07, 0.07	22.40	Na 0.8%
	Zn4	96	x, y, z	1	0.116, 0.08, 0.540	67.20	Zn 17.2%
	Pb1	32	x, x, x	3(111)	0.718, 0.718, 0.718	10.56	
OS-HY-Pb	Na2	32	x, x, x	3(111)	0.228, 0.228, 0.228	8.22	Pb 17.5%
	Na3	32	x, x, x	3(111)	0.06, 0.06, 0.06	18.85	Na 8.2%
	Na4	96	x, y, z	1	0.116, 0.08, 0.541	60.48	
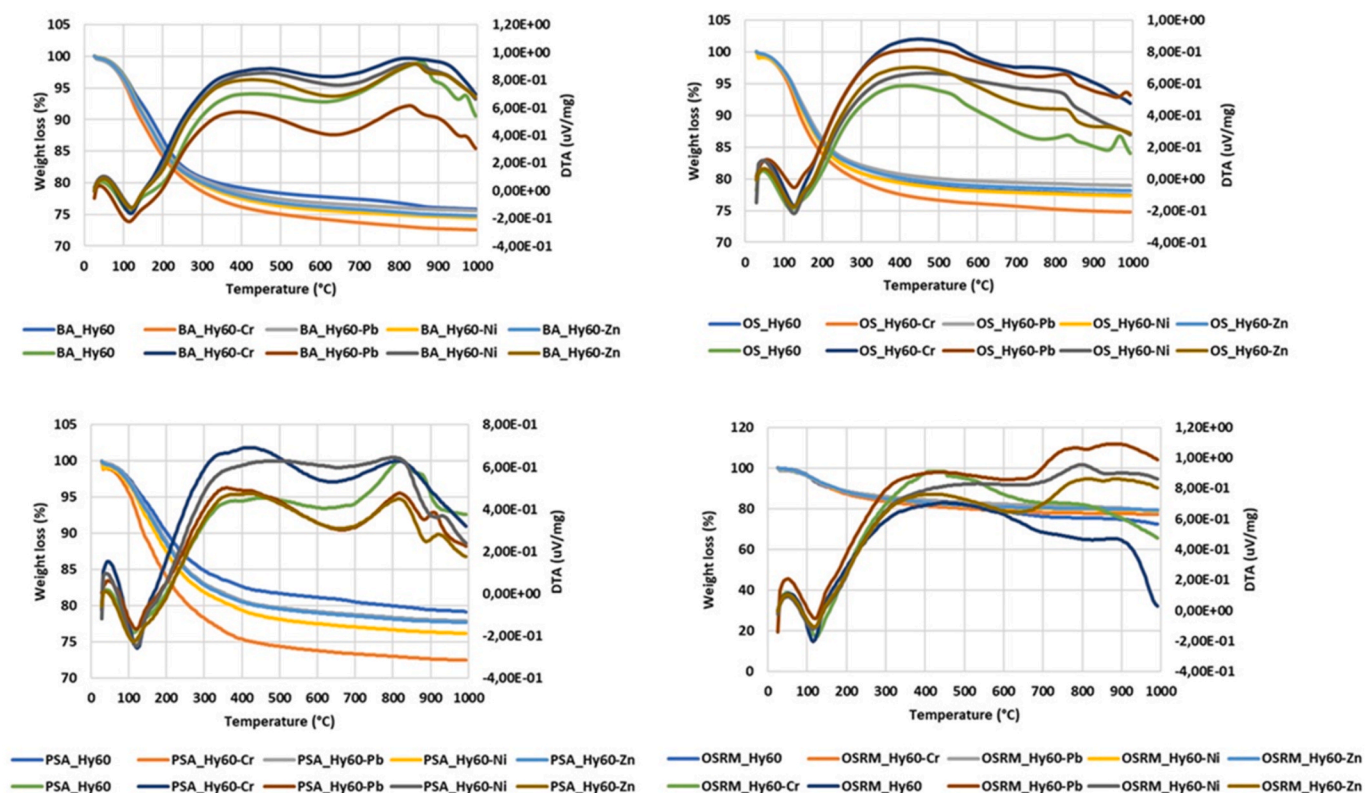
Fig. 4. TG-DTA-DSC plots of bare and metal loaded samples.

Table 3
Water content (% in weight) calculated on the basis of the Rietveld refinement and TG analyses, respectively.

Water content (weight %)	Rietveld	TG
BA-HY-60	21.63	24.14
BA-HY-Cr	23.74	27.38
BA-HY-Pb	22.47	24.39
BA-HY-Ni	21.50	25.58
BA-HY-Zn	25.69	25.22
OS_Hy60	26.6	22.60
OS_Hy60-Cr	27.00	25.18
OS_Hy60-Pb	27.96	21.08
OS_Hy60-Ni	28.11	22.71
OS_Hy60-Zn	27.39	21.87

First, the sorbent materials were rinsed with tap water to remove alkaline residuals from synthesis. Then, 20 mg of each material was suspended in 10 mL of NaNO$_3$ 0.01 M, not containing the analytes, and shaken overnight at room temperature. After that, the suspensions were centrifuged, and the pH of each solution was measured. The same experiments were also performed in the presence of each metal ion. Being the measured pH solutions around 8, a few microliters of ultrapure HNO$_3$ were added to reach a pH value around 6 to mimic actual conditions and guarantee the analytes solubilisation. In fact, the distribution species are pH-dependent, as shown by the distribution diagrams of Pb^{2+}, Zn^{2+}, Ni^{2+}, and Cr^{3+} calculated by the software Medusa (Fig. S2). The positively charged analytes are the main species at pH $\leq$ 6, while the insoluble species are predominant at pH $\geq$ 7; thus, maximum adsorption is expected around pH 6 for almost the analytes (Maraschi et al., 2018).

3.3.2. Adsorption equilibrium experiments

Two well-known empirical models, Langmuir and Freundlich, were applied to fit the experimental data and quantitatively describe the maximum metal uptake and the adsorption process onto the synthetized zeolites (Yuna, 2016; Ateia M. et al., 2021).

The Langmuir model (Eq. (4)) assumes that the adsorption process takes place on specific homogeneous sites and occurs in a monolayer on the material surface:

$$q_e = \frac{q_m K_L C_e}{1 + K_L C_e} \tag{4}$$

where K_L is the Langmuir constant and q_m the monolayer saturation capacity.

The Freundlich model describes non-ideal adsorption on the heterogeneous surface, and Eq. (5) expresses it:

$$q_e = K_F C_e^{1/n} \tag{5}$$

where K_F is the empirical constant indicative of adsorption capacity, and n is the empirical parameter representing the adsorption intensity.

As shown in Fig. 6, Zn^{2+}, Ni^{2+}, and Cr^{3+} adsorption profiles onto the investigated composites are quite different. OSRM_Hy60 is the high-performing phase, while BA_Hy60 is the less efficient one independently of the analyte considered. RM employed as alumina and magnetic nanoparticles source in the syntheses seems to affect adsorption efficiency positively: PSA_Hy60 and OSRM_Hy60 show higher adsorption capacity values than BA_Hy60 and OS_Hy60. Despite this different trend, q_{max} values fell within Pb^{2+}, Zn^{2+}, Ni^{2+}, and Cr^{3+} adsorption range reported in the literature for natural, modified, and synthetic zeolites (Yuna, 2016).

The isotherm parameters are listed in Table S5. Based on the correlation coefficient (R^2) and the good agreement between the experimental q_{max} values and the calculated ones, the Langmuir model better depicts bauxite-based composites (BA_Hy60 and PSA_Hy60) profiles, suggesting that the adsorption mechanism occurs through monolayer adsorption. Contrariwise, the Freundlich equation explains the adsorption of almost all analytes onto the heterogeneous surface of obsidian-based materials (OS_Hy60 and OSRM_Hy60).

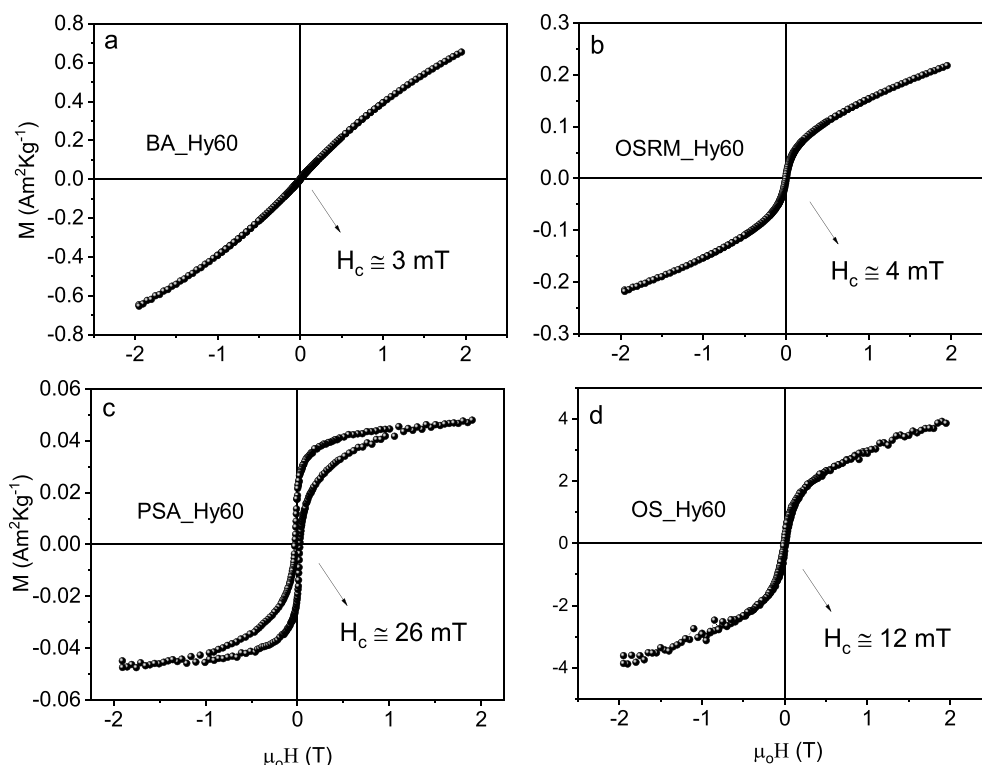In the working conditions, the measured Pb^{2+} concentration after

Fig. 5. Field dependence of magnetization recorded at 300 K of the synthetic a) BA_Hy60, b) OSRM_Hy60, c) PSA_Hy60 and d) OS_Hy60.
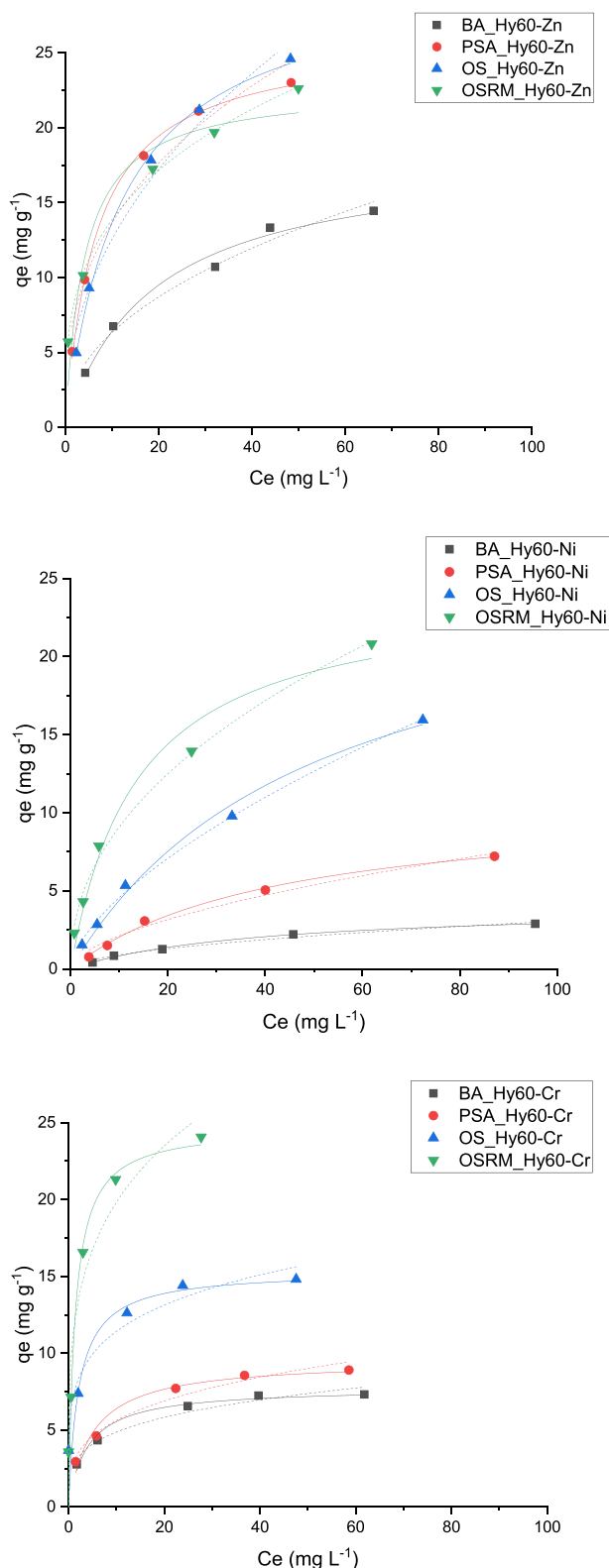
equilibration was always below the instrumental detection limit. Thus, the adsorption profiles and the thermodynamic parameters for Pb^{2+} were not detected.

3.3.3. Adsorption kinetics

Kinetic experiments were performed to determine the time required to reach the maximum adsorption of Pb^{2+}, Zn^{2+}, Ni^{2+}, and Cr^{3+}. The time-dependent data were fitted by pseudo-first-order (Eq. (6)) and pseudo-second-order kinetic (Eq. (7)) models (Yuna, 2016; Ateia M. et al., 2021):

$$q_t = q_e \left(1 - e^{k_1 t}\right) \tag{6}$$

$$q_t = \frac{q_e^2 k_2 t}{1 + q_e k_2 t} \tag{7}$$

where q_t and q_e are the metal-ions adsorbed amount at time t and equilibrium, respectively, and k_1 and k_2 are the pseudo-first-order and the pseudo-second-order rate constants.

Interestingly, Pb^{2+} uptake occurs in 5 min onto OS_Hy60 and OSRM_Hy60, 10 min onto BA_Hy60, and 30 min onto PSA_Hy60 (Fig. 7). Based on the correlation coefficient (R^2), both Equations (6) and (7) models should describe the kinetics of the process (Table S6).

For Zn^{2+}, Ni^{2+}, and Cr^{3+}, a different trend occurred. The uptake is faster onto OS_Hy60 and OSRM_Hy60 than BA_Hy60 and PSA_Hy60, but never quantitative within 4 h (Fig. S3).

Summing up, we can assume that both physisorption and chemisorption processes occur, in good agreement with the structural analysis.

3.3.4. Zeolites adsorption efficiency in actual matrices

The efficiency of BA_Hy60, PSA_Hy60, OS_Hy60, and OSRM_Hy60 for the simultaneous Pb^{2+}, Zn^{2+}, Ni^{2+}, and Cr^{3+} removal from polluted waters was evaluated following the procedure described in Paragraph 2.7.

Due to the absence of a certified reference material containing the analytes at concentration levels close to those found in contaminated waters, two water samples (tap water and WWTP effluent (Table S7) were enriched at two different metals concentration levels similar to
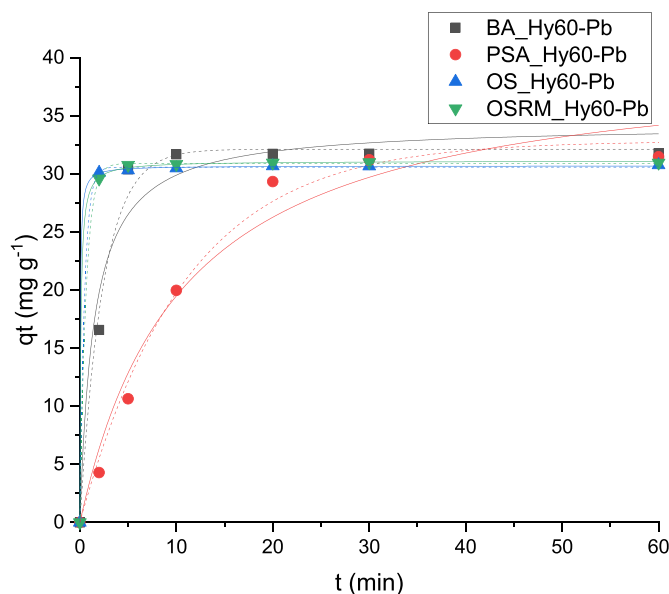
Fig. 6. Langmuir (—) and Freundlich (…) adsorption profiles for Zn, Ni, and Cr on BA_Hy60 (■black), PSA_Hy60 (● red), OS_Hy60 (▲ blue), and OSRM_Hy60 (▼ green) (Experimental conditions: sorbent 20 mg, 10 mL of NaNO₃ 0.01 M, metal-ions concentration from 25 to 200 mg L⁻¹, RSD<10%). (For interpretation of the references to colour in this figure legend, the reader is referred to the Web version of this article.)

Fig. 7. Kinetic profiles (pseudo-first-order (—), pseudo-second-order (…)) for Pb^{2+} onto BA_Hy60 (■black), PSA_Hy60 (● red), OS_Hy60 (▲ blue), and OSRM_Hy60 (▼ green) (Experimental conditions: sorbent 20 mg, 10 mL of NaNO₃ 0.01 M, Pb^{2+} initial concentration 60 mg L⁻¹, 0–60 min, RSD<10%). (For interpretation of the references to colour in this figure legend, the reader is referred to the Web version of this article.)

those found in polluted natural waters and industrial wastewater (Meng et al., 2017). As shown in Fig. 8, BA_Hy60 and PSA_Hy60 have a similar trend in both matrices: a good adsorption efficiency is obtained in samples spiked at low-level concentrations, while Ni^{2+} and Zn^{2+} are not quantitatively removed at high concentrations. On the contrary, the performances of OS_Hy60 and OSRM_Hy60 differ depending on the matrix composition and the analytes concentrations. Unlike OS_Hy60, OSRM_Hy60 guaranteed a satisfactory removal of all the analytes at different concentrations in both matrices. These results underline the crucial role of RM in the metal-ions adsorption, also in the presence of matrix constituents.

3.3.5. Metal-ions and zeolite structure

Despite FTIR spectra of the zeolite samples before and after metal adsorption are comparable (S4), X-ray diffraction peaks profiles, instead, reveal modifications of both position and intensities, as shown in Fig. 9. In all samples, the same symmetry was maintained before and after adsorption and modifications of both unit lattice parameters (Table 4) and crystallite size (Table S4) as respect to the as-synthetized materials are detected. The polyphase nature of PSA_Hy60 and OSRM_Hy60 samples hampered structure refinements to prove a

variation of the extra-framework population before and after metal-ions loading, and just BA_Hy60 and OS_Hy60 are possible to evaluate.

After contact with the Pb^{2+}, Zn^{2+}, Ni^{2+}, and Cr^{3+} solutions at a concentration corresponding to the maximum metal adsorption uptake, despite some variations in the relative intensity (ascribable to modification of the electronic density inside the pores) of the powder diffraction reflection, any significant modifications of the zeolites crystallinity are observed on both zeolites. The dissolved cations are removed from the solution through an 'ion-exchange' mechanism (immobilization of cations into the channels of the tetrahedral framework) (Godelitsas and Armbruster, 2003), which modifies the initial zeolite structures in terms of dimension of the unit cell volume, total pore volume (TPV), water content and extra-framework cations composition. The Rietveld refinements allow us to determine the extra-framework positions of both charge-compensating cations and water molecules (Table 2, Table S1). A good agreement and consistency of the refined extraframework charges and the Si/Al ratio of the parent zeolites (Table S1) is observed. Considering the results obtained from the structure refinements, the Na1 (in BA_Hy60) and Na3 (in OS_HY60) sites represent the atomic site positions maintained by residual Na^+ cations in partially exchanged zeolites. In BA_Hy60, Zn^{2+}, Ni^{2+}, and Cr^{3+} ions occupy just one position at
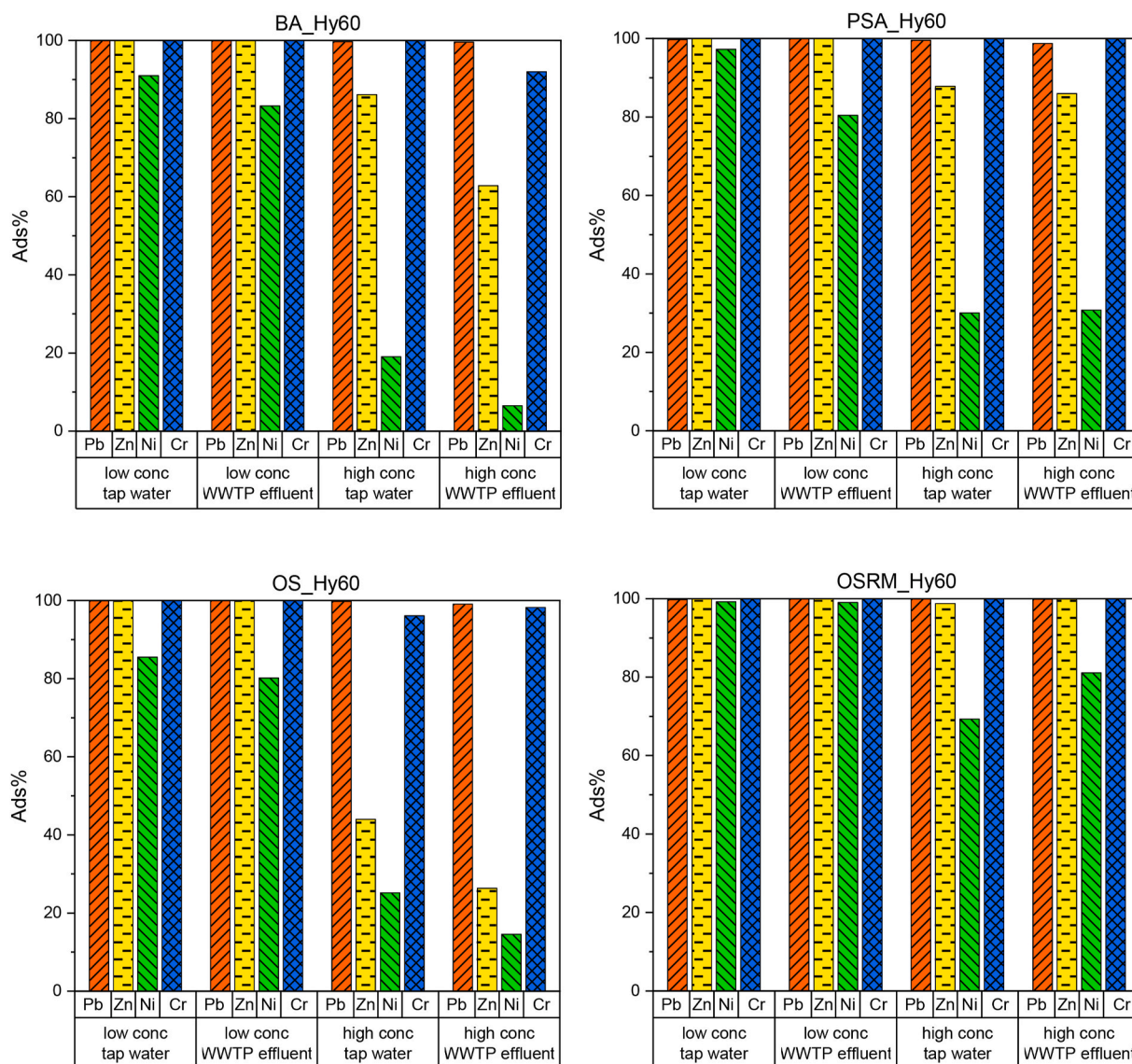

Fig. 8. Adsorption efficiency of BA_Hy60, PSA_Hy60, OS_Hy60, and OSRM_Hy60 toward Pb^{2+}, Zn^{2+}, Ni^{2+}, and Cr^{3+} (Experimental conditions: sorbent 20 mg, 10 mL water sample spiked with Pb^{2+}, Zn^{2+}, Ni^{2+}, and Cr^{3+} 3–6 mg L^{-1} (low concentration) and 50–87 mg L^{-1} (high concentration), RSD< 10%).
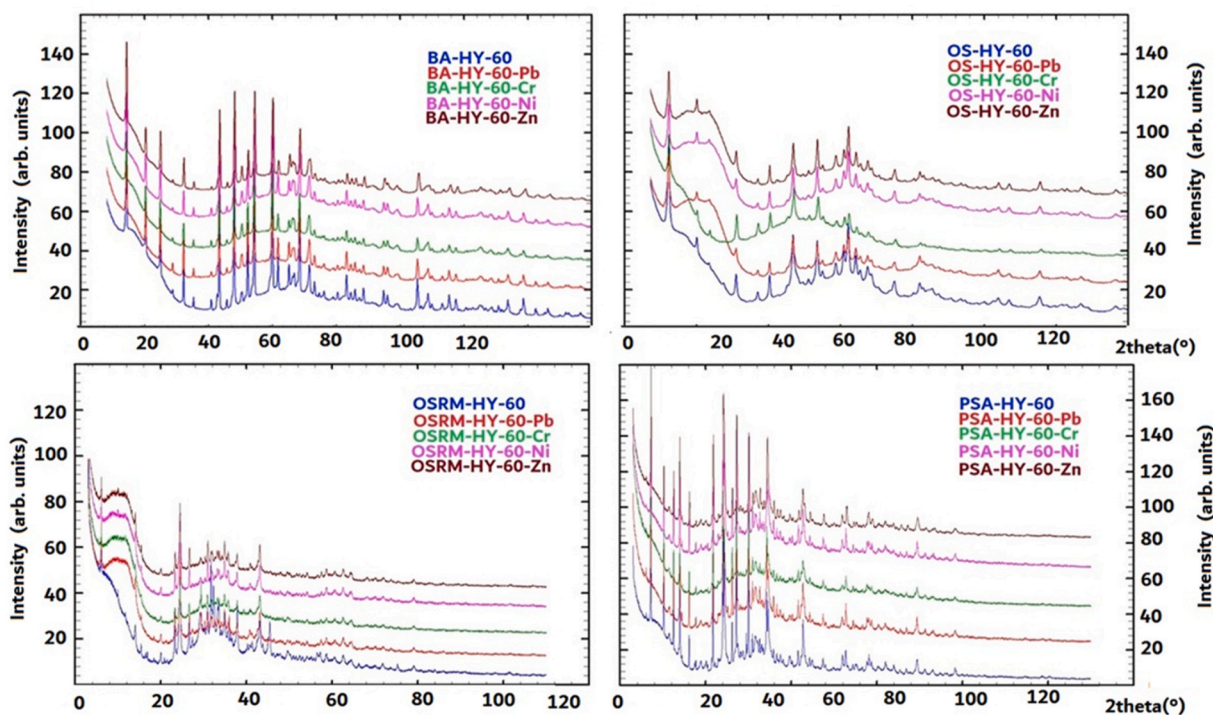
Fig. 9. X-ray powders diffraction patterns of bare and metal loaded samples.

Table 4
Lattice parameters for selected zeolites before and after heavy metals adsorption. Refined 3–110° 2θ range. Wavelength (Å) 1.540593 Cu Kα1, and 1.544427 Cu Kα2.

Sample	Space Group	a = b = c (Å)	V (Å3)
BA_Hy60	P m −3 m	12.265(2)	1845.1(1)
BA_Hy60-Cr	P m −3 m	12.264(3)	1844.4(1)
BA_Hy60-Pb	P m −3 m	12.268(2)	1.846.1(4)
BA_Hy60-Ni	P m −3 m	12.265(1)	1844.9(2)
BA_Hy60-Zn	P m −3 m	12.229(6)	1828.7(1)
OS_Hy60	F d −3	24.904(2)	15445.7(2)
OS_Hy60-Cr	F d −3	24.830(3)	15308.9(3)
OS_Hy60-Pb	F d −3	24.908(7)	15452.9(8)
OS_Hy60-Ni	F d −3	24.894(3)	15426.9(5)
OS_Hy60-Zn	F d −3	24.876(2)	15394.0(9)
PSA_Hy60 + SODALITE	F m −3 c P −4 3 m	24.545(1) 9.002(1)	14786.5(1) 729.6(1)
PSA_Hy60-Cr + SODALITE	F m −3 c P −4 3 m	24.526(1) 8.911(2)	14753.8 (13) 707.6(3)
PSA_Hy60-Pb + SODALITE	F m −3 c P −4 3 m	24.499(1) 8.995(1)	14704.2(1) 727.8(2)
PSA_Hy60-Ni + SODALITE	F m −3 c P −4 3 m	24.491(2) 9.011(2)	14690.7(5) 731.7(1)
PSA_Hy60-Zn + SODALITE	F m −3 c P −4 3 m	24.502(1) 8.993(2)	14710.3(1) 727.4(1)
OSRM_Hy60 + SODALITE	F d −3 P -4 3 m	24.974(32) 8.875(4)	15576.2(3) 699.0(1)
OSRM_Hy60-Cr + SODALITE	F d −3 P -4 3 m	24.947(5) 8.891(4)	15525.7(5) 702.9(1)
OSRM_Hy60-Pb + SODALITE	F d −3 P -4 3 m	24.946(1) 8.880(3)	15524.4(2) 700.1(4)
OSRM_Hy60-Ni + SODALITE	F d −3 P -4 3 m	24.958(1) 8.867(1)	15546.5(1) 697.1(1)
OSRM_Hy60-Zn + SODALITE	F d −3 P -4 3 m	24.937(1) 8.876(1)	15506.7(2) 699.34(7)

x, y, y, representing the only extraframework cationic site not interacting with the framework oxygens atoms (Table S1). In OS_HY60, site1 at the centre of the hexagonal window (Table S1) does not interact with the framework and appears to be the preferred site for all exchanged ions.

Consequently, based on XRPD Rietveld analysis, it is found that host–guest interactions between the framework oxygen atoms, co-adsorbed water molecules, and cations limit the diffusion of heavy metals inside the zeolite channel systems, controlling the location of cations during the ion-exchange process. Therefore, the difficulty for successful metal-loading can be ascribed to several factors such as the Si/Al ratio, the degree of tetrahedral (Si, Al) ordering, the ionic potential Z/r (where Z and r were the nominal charge and radius of exchangeable cations, respectively), the effect of pH and temperature, the solid/liquid ratio, the zeolite surface and finally, the treatment time and the renewals of the solution (Godelitsas and Armbruster, 2003; Sani et al., 1999; Bresciani-Pahor et al., 1980; Shepelev et al., 1991; Borissenko et al., 2008). Complete metal-ions exchange is only achieved in BA_Hy60 loaded with Pb: the crystallographic sites refined with Pb scattering curves give rise to ~5 Pb^{2+} cations and 43 water molecules in BA_Hy60-Pb corresponding to ~36 and ~22% in weight, respectively (Table 2). The adsorption of metal ions in the zeolite channels is also confirmed by the porosity variations (Table 5). When calculating filled space and hence,

Table 5
Ba-HY-60 and OS-HY-60 zeolite channels porosity before and after metal ionsadsorption.

Sample	Unit cell Volume	Filled space per unit cell	Void space per unit cell
BA_HY-60	1845.06 Å3	782.46 Å3 (42.41%)	1062.60 Å3 (57.59%)
BA_HY-Cr	1844.45 Å3	625.56 Å3 (33.92%)	1218.89 Å3 (66.08%)
BA_HY-Pb	1846.13 Å3	966.13 Å3 (52.33%)	880.00 Å3 (47.67%)
BA_HY-Ni	1844.91 Å3	622.20 Å3 (33.73%)	1222.71 Å3 (66.27%)
BA_HY-Zn	1828.69 Å3	808.94 Å3 (44.24%)	1019.75 Å3 (55.76%)
OS_Hy60	15445.73 Å3	6483.46 Å3 (41.98%)	8962.27 Å3 (58.02%)
OS_Hy60-Cr	15308.87 Å3	6200.60 Å3 (40.50%)	9108.28 Å3 (59.50%)
OS_Hy60-Pb	15452.88 Å3	6881.79 Å3 (44.53%)	8571.09 Å3 (55.47%)
OS_Hy60-Ni	15423.54 Å3	5727.20 Å3 (37.13%)	9696.34 Å3 (62.87%)
OS_Hy60-Zn	15394.03 Å3	5705.96 Å3 (37.07%)	9688.07 Å3 (62.93%)

the percentage of free space, the nature and especially the dimensions of the cations must be taken into account. It is evident that the introduction of large cations (such as Pb) promoted a decrease on the void space per unit cell. This effect can be ascribed to the occurrence of hydrated metal ions in the zeolite channels/cavities, thus determining a decrease on the micropore area. The drop on the micropore area is more appreciable as the ion-exchange level increases due to a greater blocking effect on micropores.

The refined water content is in good agreement with the mass loss

registered by the TG curves (Fig. 4). After Pb^{2+}, Zn^{2+}, Ni^{2+}, Cr^{3+} adsorption, all thermograms showed a first water departure in the 60–150 °C range due to the weakly-bound water, and another weight loss in the 150–250 °C range due to the water located in zeolite cavities interacting with the extraframework cations. At the same time, the high-temperature DTA peak for metal-exchanged zeolites is shifted towards lower temperature by about 10–30 °C, thus indicating different host-guest interactions after metal ions exchange. The position of this latter DTA peak depends on the nature of the extraframework cations: cations
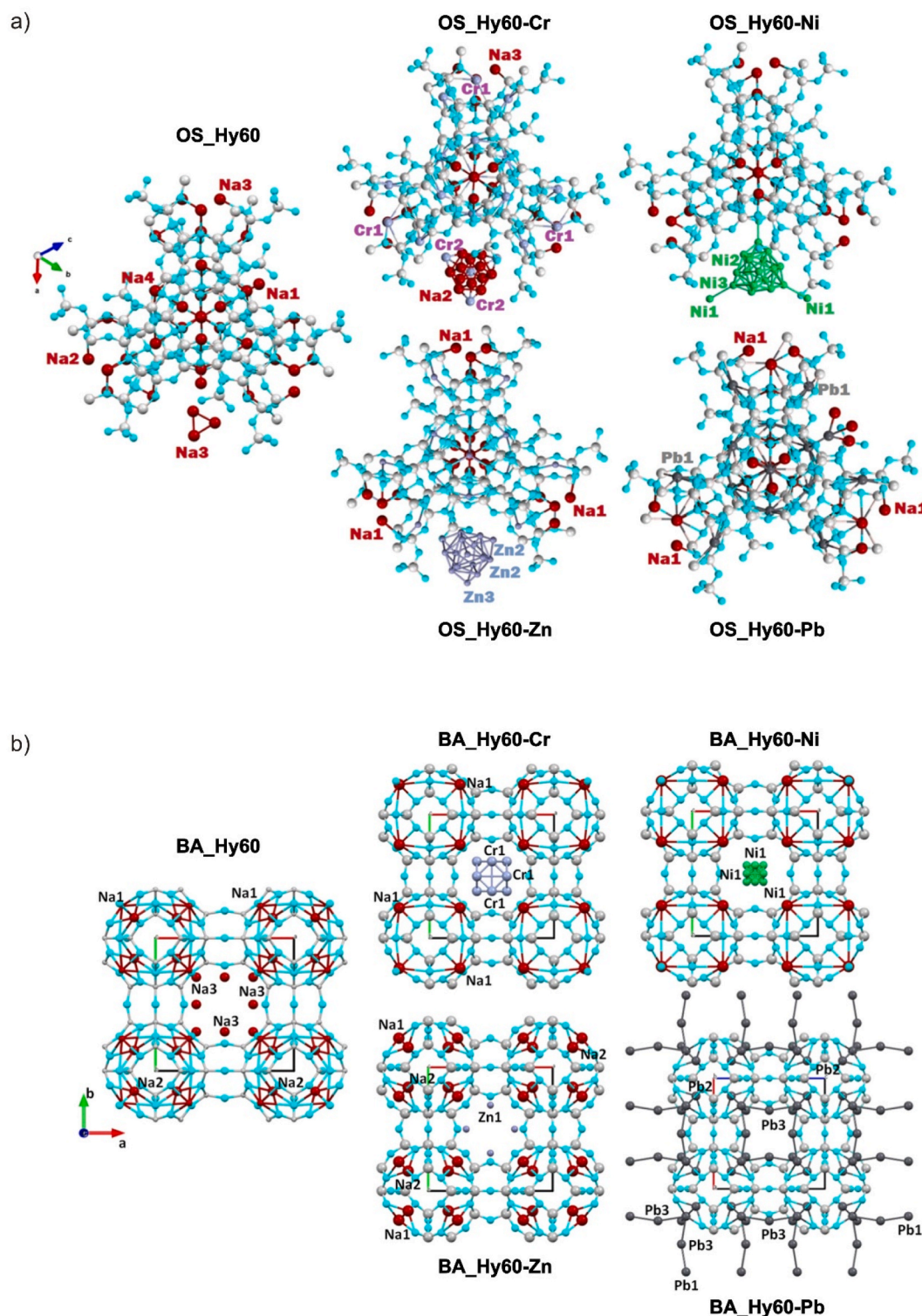

Fig. 10. Locations of metal-ions in a) OS_Hy60 and b) BA_Hy60 samples.

with a higher charge interact greatly with the H_2O molecules, thus favouring the formation of hydrogen bonds between water molecules and the framework oxygen atoms. Consequently, the interactions between the framework oxygen and water appear stronger in the zeolite exchanged with bivalent ions. In addition, the large cations show less zeolite water loss (sum of the weakly-bound water and metal-bound) since the greater the size of the exchangeable cation, the smaller is the space for the extraframework water molecules (Fig. 4). In addition, a last exothermic peak is appeared on DTA curves at higher temperatures (900–1000 °C) due to zeolite destruction and crystallization of new phases.

The extra-framework metal-cations exchanged with Na^+ are located on crystallographic sites corresponding to the extra-framework positions of the pristine zeolites, and their coordination polyhedra are similar to those of the natural phases, except for bond distances (Fig. 10). The accuracy of the refined occupancy of a specific extra-framework site is strongly depended on the number of electrons of the chemical species and its either static or dynamic translational disorder. On the whole, the Rietveld method gives an extra-framework cations content that fits well with the saturation capacity determined by the adsorption isotherm (see Weight % from Rietveld and Weight % from adsorption isotherms in Table 2, S5, and Fig. 6).

3.3.6. Preliminary tests on the synthetic zeolite reuse

Reusability of each zeolite was evaluated in the presence of a mixture of Pb^{2+}, Zn^{2+}, Ni^{2+}, and Cr^{3+} for three cycles, following the procedure described in Paragraph 2.7 (20 mg sorbent material, 10 mL of spiked tap

water with Pb^{2+}, Zn^{2+}, Ni^{2+}, and Cr^{3+} 2–4 mg L^{-1}, native pH, 24 h contact). After equilibration, each supernatant was separated and analyzed by ICP-OES for the heavy metals content, while the sorbent phase was submitted for further adsorption.

Fig. 11 shows the adsorbed metals percentage, calculated by Eq. (3) after each adsorption cycle. After three consecutive adsorption cycles, a quantitative removal (>96%) of Pb^{2+}, Zn^{2+}, and Cr^{3+} was obtained for all the investigated zeolites. A slightly different trend was observed for Ni^{2+}. BA_Hy60 and PSA_Hy60 removed around 70% of Ni^{2+} in each adsorption cycle, OS_Hy60 and OSRM_Hy60 were more efficient in the first two treatment cycles. OSRM_Hy60 is the most performing material.

4. Conclusion

The results show that zeolite X, sodalite, and zeolite A, simply formed from natural sources, bauxite, and obsidian, also combined with waste material (red mud), can absorb heavy metals. Thermodynamic data differ depending on the zeolite types, while the kinetic ones vary as a function of the considered analyte. Nevertheless, the toxic metals adsorption mechanism is due to the ion exchange and the precipitation onto the synthetic zeolites. Based on XRPD Rietveld analysis, it is found that host–guest interactions between the framework oxygen atoms, co-adsorbed water molecules, and cations take place inside the zeolite channels, according to the type of the newly-formed mineral. Their occurrence controls the diffusion of heavy metals inside the zeolite channel systems, as well as the location of cations during the ion exchange process. This finding suggests that the cation exchange
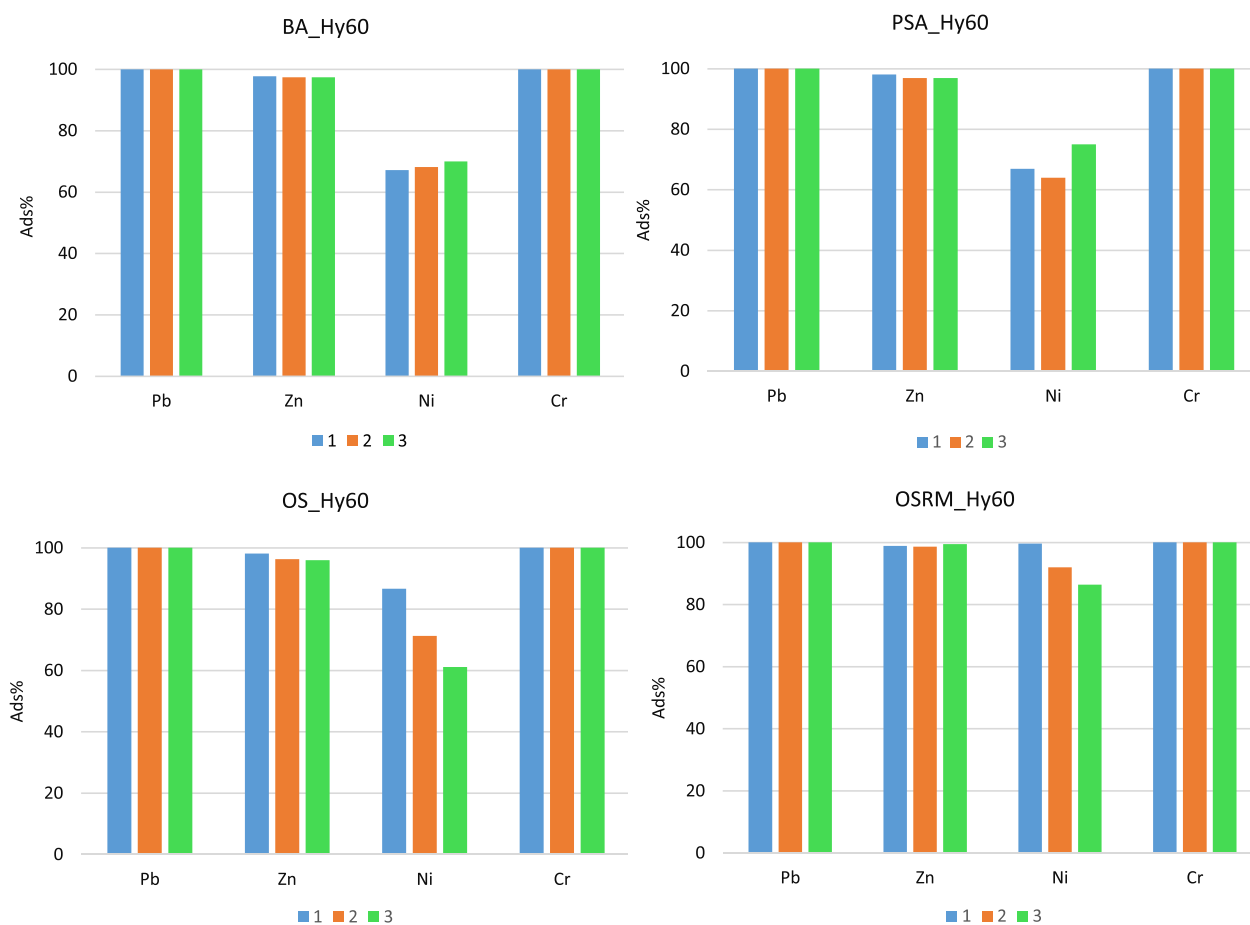

Fig. 11. Influence of the number of adsorption cycles on BA_Hy60, PSA_Hy60, OS_Hy60, and OSRM_Hy60 (Experimental conditions: sorbent 20 mg, 10 mL tap water spiked with Pb^{2+}, Zn^{2+}, Ni^{2+}, and Cr^{3+} 2–4 mg L^{-1}).

properties of zeolite are not predictable only based on the ionic radius of cations but also on the host-guest interactions.

Their magnetic properties and their adsorption capability under relevant environmental conditions, make these zeolites excellent candidates for heavy metals removal from polluted water.

Credit author statement

Claudia Belviso: Conceptualization, Investigation, Formal analysis, Writing – original draft, Writing – review & editing; **Paola Lucini**: Formal analysis; **Maura Mancinelli**: Formal analysis; **Maryam Abdolrahimi**: Formal analysis; **Annalisa Martucci**: Investigation, Formal analysis, Writing – original draft; Writing – review & editing, **Davide Peddis**: Investigation, Writing – original draft; **Federica Maraschi**: Formal analysis; **Francesco Cavalcante**: Writing – original draft; **Michela Sturini**: Conceptualization, Investigation, Formal analysis, Writing – original draft; Writing – review & editing.

Declaration of competing interest

The authors declare that they have no known competing financial interests or personal relationships that could have appeared to influence the work reported in this paper.

Data availability

No data was used for the research described in the article.

Acknowledgments

Appendix A. Supplementary data

Supplementary data to this article can be found online at https://doi.org/10.1016/j.jclepro.2023.137814.

References

Abatal, M., Olguin, M.T., Abdellaoui, Y., Bouari, A.E.L., 2018. Sorption Cd (II) and Ni (II) on natural, sodium-, and acid-modified clinoptilolite-rich tuff. Environ. Protect. Eng. 44, 41–59.

Abdelrahman, E.A., Abou El-Reash, Y.G., Youssef, H.M., Kotp, Y.H., Hegazey, R.M., 2021. Utilization of rice husk and waste aluminum cans for the synthesis of some nanosized zeolite, zeolite/zeolite, and geopolymer/zeolite products for the efficient removal of Co(II), Cu(II), and Zn(II) ions from aqueous media. J. Hazard. Mater. 401, 123813.

Alberti, S., Caratto, V., Peddis, D., Belviso, C., Ferretti, M., 2019. Synthesis and characterization of a new photocatalyst based on TiO₂ nanoparticles supported on a magnetic zeolite obtained from iron and steel industrial waste. J. Alloys Compd. 797, 820–825.

Ateia, M., Helbling, D.E., Dichtel, W.R., 2021. Best practices for evaluating new materials as adsorbents for water treatment. ACS Mater. Lett. 2, 1532–1544.

Belviso, C., 2016. EMT-type zeolite synthesized from obsidian. Microporous Mesoporous Mater. 226, 325–330.

Belviso, C., Cavalcante, F., Di Gennaro, S., Lettino, A., Palma, A., Ragone, P., Fiore, S., 2014. Removal of Mn from aqueous solution using fly ash and its hydrothermal synthetic zeolite. J. Environ. Manag. 137, 16–22.

Belviso, C., Agostinelli, E., Belviso, S., Cavalcante, F., Pascucci, S., Peddis, D., Varvaro, G., Fiore, S., 2015. Synthesis of magnetic zeolite at low temperature using a waste material mixture: fly ash and red mud. Microporous Mesoporous Mater. 202, 208–216.

Belviso, S., Cavalcante, F., Lettino, A., Ragone, P., Belviso, C., 2016. Fly ash as raw material for the synthesis of zeolite-encapsulated porphyrazine and metallo porphyrazine tetrapyrrolic macrocycles. Microporous Mesoporous Mater. 236, 328-234.

Belviso, C., Kharchenko, A., Agostinelli, E., Cavalcante, F., Peddis, D., Varvaro, G., Yaacoub, N., Mintova, S., 2018. Red mud as aluminium source for the synthesis of magnetic zeolite. Microporous Mesoporous Mater. 270, 24–29.

Belviso, C., Peddis, D., Varvaro, G., Abdolrahimi, M., Reverberi, A.P., Cavalcante, F., 2020a. Obsidian as a raw material for eco-friendly synthesis of magnetic zeolites. Materials 13, 4633.

Belviso, C., Piancastelli, A., Sturini, M., Belviso, S., 2020b. Synthesis of composite zeolitelayered double hydroxides using ultrasonic neutralized red mud. Microporous Mesoporous Mater. 299, 110108.

Belviso, C., Cannas, C., Pinna, N., Cavalcante, F., Lettino, A., Lotti, P., Gatta, D., 2020c. Effect of red mud added to zeolite LTA synthesis: where is Fe in the newly-formed material? Microporous Mesoporous Mater. 298, 110058.

Belviso, C., Abdolrahimi, M., Peddis, D., Gagliano, E., Sgroi, M., Lettino, A., Roccaro, P., Vagliasindi, F.G.A., Falciglia, P.P., Di Bella, G., Giustra, M.G., Cavalcante, F., 2021. Synthesis of zeolite from volcanic ash: characterization and application for cesium removal. Microporous Mesoporous Mater. 319, 111045.

Belviso, C., Mancinelli, M., Lettino, A., 2022. A green process for zeolite synthesis: low temperature vapor phase treatment of natural bauxites. J. Mater. Sci. 57, 16619–16631.

Borissenko, E., Porcher, F., Bouché, A., Lecomte, C., Souhassou, M., 2008. Single crystal structure of fully dehydrated partially Co2+-exchanged zeolite X: comparison with partially dehydrated partially Co2+-exchanged zeolites X. Microporous Mesoporous Mater. 114 (1–3), 155–165.

Bresciani-Pahor, N., Calligaris, M., Nardin, G., Randaccio, L., Russo, E., Comin-Chiaramonti, P., 1980. Crystal structure of a natural and a partially silver-exchanged heulandite. J. Chem. Soc., Dalton Trans. 9, 1511–1514.

Cheng, Y., Xu, L., Jiang, Z., Liu, C., Zhang, Q., Zou, Y., Chen, Y., Li, J., Liu, X., 2020. Feasible low-cost conversion of red mud into magnetically separated and recycled hybrid SrFe12O19@ NaP1 zeolite as a novel wastewater adsorbent. Chem. Eng. J. 417, 128090.

Choi, Y.S., Lee, M.S., Oh, S.H., 2002. Manufacturing Method of Zeolite 4A Using Bauxite. KR Patent 094527-A; 415941-B.

Chuenpratoom, T., Hemavibool, K., Rermthong, K., Nanan, S., 2021. Removal of lead by merlinoite prepared from sugarcane bagasse ash and kaolin: synthesis, isotherm, kinetic, and thermodynamic studies. Molecules 26, 7550.

Coombs, D.S., Alberti, A., Armbruster, T., Artioli, G., Colella, C., Galli, E., Grice, D., Liebau, F., Mandarino, J.A., Minato, H., Nickel, E.H., Passaglia, E., Peacor, D.R., Quartieri, S., Rinaldi, R., Ross, M., Sheppard, R., Tillmanns, E., Vezzalini, G., 1997. Recommended nomenclature for zeolite minerals: report of the subcommittee on zeolites of the international mineralogical association, commission on new minerals and mineral names. Can. Mineral. 35, 1571–1606.

Finger, L.W., Cox, D.E., Jephcoat, A.P., 1994. A correction for powder diffraction peak asymmetry due to axial divergence. J. Appl. Crystallogr. 27, 892–900.

Fu, H., Li, Y., Yu, Z., Shen, J., Li, J., Zhang, M., Ding, T., Xu, L., 2020. Ammoniumremoval using a calcined. Natural zeolite modified with sodium nitrate, 393, 122481.

Gao, R., Liu, B., Xu, Z., 2019. Fabrication of magnetic zeolite coated with carbon fiber using pyrolysis products from waste printed circuit boards. J. Clean. Prod. 231, 1149–1157.

Godelitsas, A., Armbruster, T., 2003. HEU-type zeolites modified by transition elements and lead. Microporous Mesoporous Mater. 61 (1–3), 3–24.

Gualtieri, A., Norby, P., Artioli, G., Hanson, J., 1997. Kinetics of formation of zeolite Na-A [LTA] from natural kaolinites. Phys. Chem. Miner. 24, 191–199.

He, M., Zhu, Y., Yang, Y., Han, B., Zhang, Y., 2011. Adsorption of cobalt(II) ions from aqueous solutions by palygorskite. Appl. Clay Sci. 54, 292.

He, Y., Tang, S., Yin, S., Li, S., 2021. Research progress on green synthesis of various high-purity zeolites from natural material-kaolin. J. Clean. Prod. 306, 127248.

Hussain, T., Hussain, A.I., Shahid Chatha, S.A., Ali, A., Rizwan, M., Ali, S., Ahamd, P., Wijaya, L., Alyemeni, M.N., 2021. Synthesis and characterization of Na-zeolites from textile waste ash and its application for removal of lead (Pb) from wastewater. Int. J. Environ. Res. Publ. Health 18, 3373.

Inyang, M.I., Gao, B., Yao, Y., Xue, Y., Zimmerman, A., Mosa, A., Cao, X., 2016. A review of biochar as a low-cost adsorbent for aqueous heavy metal removal. Crit. Rev. Environ. Sci. Technol. 46, 406–433.

Jiang, M.Q., Jin, X.Y., Lu, X.Q., Chen, Z.L., 2010. Adsorption of Pb(II), Cd(II), Ni(II) and Cu(II) onto natural kaolinite clay. Desalination 252, 33–39.

Jiang, Z.X., Liu, Q.S., Barron, V., Torrent, J., Yu, Y., 2012. Magnetic dis-crimination between Al-substituted hematites synthesized by hydrothermal and thermal dehydration methods and its geological significance. J. Geophys. Res. 117, B02102.

Jiang, Z., Liu, Q., Zhao, X., Jin, C., Liu, C., Li, S., 2015. Thermal magnetic behaviour of Al-substituted haematite mixed with clay minerals and its geological significance. Geophys. J. Int. 200, 130–143.

Jinendra, U., Kumar, J., Nagabhushana, B.M., Raghu, A.V., Bilehal, D., 2019a. Facile synthesis of CoFe₂O₄ nanoparticles and application in removal of malachite green dye. Green Mater. 7, 137–142.

Jinendra, U., Bilehal, D., Nagabhushana, B.M., Reddy, K.R., Reddy, C.V., Raghu, A.V., 2019b. Template-free hydrothermal synthesis of hexa ferrite nanoparticles and its adsorption capability for different organic dyes: comparative adsorption studies, isotherms and kinetic studies. Mat. Sci. En. Techn. 2, 657–666.

Jyothi, M.S., Nayak, V., Reddy, K.R., Naveen, S., Raghu, A.V., 2019. Nanophotocatalysis and environmental applications. In: Sharma, G., Kumar, A., Lichtfouse, E., Asiri, A. M. (Eds.), Materials and Technology. Springer Cham, New York, p. 83, 2019.

Kareem, A., Dawagreh, M.A., 2017. Removal of zinc from wastewater by using Jordanian natural zeolite. Asian J. Microbiol. Biotechnol. Environ. Sci. 19, 625.

Kiruba, U.P., Kumar, P.S., Prabhakaran, C., Aditya, V., 2014. Characteristics of thermodynamic, isotherm, kinetic, mechanism and design equations for the analysis of Adsorption in Cd (II) ions-surface modified Eucalyptus seeds system. J. Taiwan Inst. Chem. Eng. 45, 2957–2968.

Kozara-Sucharda, B., Gworek, B., Kondzielski, Igor, 2020. The simultaneous removal of zinc and cadmium from multicomponent aqueous solutions by their sorption onto selected natural and synthetic zeolites. Minerals 10, 343.

Kuang, H., Yuancai, C., Zhenghua, T., Yongyou, H., 2015. Removal of heavy metal ions from aqueous solution by zeolite synthesized from fly ash. Environ. Sci. Pollut. Res. 23, 2778–2788.

Kuroki, S., Hashishinb, T., Morikawad, T., Yamashitad, K., Matsuda, M., 2019. Selective synthesis of zeolites A and X from two industrial wastes: crushed stone powder and aluminum ash. J. Environ. Manag. 231, 749–756.

Larson, A.C., Von Dreele, R.B., 2000. General Structure Analysis System (GSAS) Report LAUR 86-748. Los Alamos National Laboratory, Los Alamos.

Liu, S., Ding, Y., Li, P., Diao, K., Tan, X., Lei, F., Zhan, Y., Li, Q., Huang, B., Huang, Z., 2014. Adsorption of the anionic dye Congo red from aqueous solution onto natural zeolites modified with N, N-dimethyl dehydroabietylamine oxide. Chem. Eng. J. 248, 135–144.

Mameli, V., Musinu, A., Niznansky, D., Peddis, D., Ennas, G., Ardu, A., Lugliè, C., Cannas, C., 2016. Much more than a glass: the complex magnetic and microstructural properties of obsidian. J. Phys. Chem. 120, 27635–27645.

Mancinelli, M., Arfè, A., Martucci, A., Pasti, L., Chenet, T., Sarti, E., Vergine, G., Belviso, C., 2020. Evaluation for the removal efficiency of VOCs and heavy metals by zeolites-based materials in the wastewater: a case study in the Tito Scalo industrial area. Processes 8, 1519.

Maraschi, F., Speltini, A., Tavani, T., Gulotta, M.G., Dondi, D., Milanese, C., Prato, M., Profumo, A., Sturini, M., 2018. Silica-supported pyrolyzed lignin for solid-phase extraction of rare earth elements from fresh and sea waters followed by ICP-MS detection. Anal. Bioanal. Chem. 410, 7635–7643.

Meng, L., Li, X., Wang, X., Ma, K., Liu, G., Zhang, J., 2017. Amoxicillin effects on functional microbial community and spread of antibiotic resistance genes in amoxicillin manufacture wastewater treatment system. J. Environ. Sci. 61, 110–117.

Mezni, M., Hamzaoui, A., Hamdi, N., Srasra, E., 2011. Synthesis of zeolites from the low-grade Tunisian natural illite by two different methods. Appl. Clay Sci. 1, 209–218.

Momma, K., Izumi, F., 2011. VESTA 3 for three-dimensional visualization of crystal, volumetric and morphology data. J. Appl. Crystallogr. 44, 1272–1276.

Motoharu, K., Katsutoshi, T., 1997. Experimental study on the formation of zeolites from obsidian by interaction with NaOH and KOH solutions at 150 and 200 °C. Clay Clay Miner. 45, 365–377.

Murad, E., Schwertmann, U., 1986. Influence of A1 substitution and crystal size on the room-temperature Mossbauer spectrum of hematite. Clay Clay Miner. 34, 1–6.

Ng, E.-P., Awala, H., Tan, K.H., Adam, F., Retoux, R., Mintova, S., 2015. EMT-type zeolite nanocrystals synthesized from rice husk. Microporous Mesoporous Mater. 204, 2014–2209.

Ozdes, D., Duran, C., Senturk, H.B., 2011. Adsorptive removal of Cd(II) and Pb(II) ions from aqueous solutions by using Turkish illitic clay. J. Environ. Manag. 92, 3082.

Psycharis, V., Perdikatsis, V., Christidis, G., 2004. Crystal structure and Rietveld refinement of zeolite A synthesized from fine-grained perlite waste materials. Bull. Geol. Soc. Greece 36, 121–129.

Ren, Z., Wang, L., Li, Y., Zha, J., Tian, G., Wang, F., Zhang, H., Liang, J., 2022. Synthesis of zeolites by in-situ conversion of geopolymers and their performance of heavy metal ion removal in wastewater: a review. J. Clean. Prod. 349, 131441.

Salman, H., Shaheen, H., Abbas, G., Khalouf, N., 2017. Use of Syrian natural zeolite for heavy metals removal from industrial waste water: factors and mechanism. J. Entomol. Zool. Stud. 5, 452.

Sani, A., Vezzalini, G., Ciambelli, P., Rapacciuolo, M.T., 1999. Crystal structure of hydrated and partially NH4-exchanged heulandite. Microporous Mesoporous Mater. 31 (3), 263–270.

Saravanan, A., Sundararaman, T.R., Jeevanantham, S., Karishma, S., Kumar, P.S., Yaashikaa, P.R., 2020. Effective Adsorption of Cu (II) ions on sustainable adsorbent derived from mixed biomass (Aspergillus campestris and agro waste): optimization, isotherm and kinetics study. Groundw. Sustain. Dev. 11, 100460.

Sen, T.K., Gomez, D., 2011. Adsorption of zinc (Zn^{2+}) from aqueous solution on natural bentonite. Desalination 267, 286.

Senthil Kumar, P., Sivaranjanee, R., Sundar Rajan, P., Saravanan, A., 2018. Carbon sphere: synthesis, characterization and elimination of toxic Cr (VI) ions from aquatic system. J. Ind. Eng. Chem. 60, 307–320.

Shawabkeh, R., Al-Harahsheh, A., Hami, M., Khlaifat, A., 2004. Conversion of oil shale ash into zeolite for cadmium and lead removal from wastewater. Fuel 83, 981–985.

Shepelev, Y.F., Butikova, I.K., Smolin, Y.I., 1991. Crystal structures of the partially K-, Rb-, and Cs-exchanged forms of NaX zeolite in both the hydrated and the dehydrated (400 C) states. Zeolites 11 (3), 287–292.

Sprynskyy, M., Buszewski, B., Terzyk, A.P., Namiesnik, J., 2006. Study of the selection mechanism of heavy metal (Pb^{2+}, Cu^{2+}, Ni^{2+}, and Cd^{2+}) adsorption on clinoptilolite. J. Colloid Interface Sci. 304, 21–28, 2006.

Srivastava, S., Agrawal, S.B., Mondal, M.K., 2015. A review on progress of heavy metal removal using adsorbents of microbial and plant origin. Environ. Sci. Pollut. Res. 22, 15386–15415.

Suber, L., Imperatori, P., Mari, A., Marchegiani, G., Mansilla, M.V., Fiorani, D., Plunkett, W.R., Rinaldi, D., Cannas, C., Ennas, G., Peddis, D., 2010. Thermal hysteresis of Morin transition in hematite particles. Phys. Chem. Chem. Phys. 12, 6984–6989.

Sun, J.M., Shang, C., Huang, J.C., 2003. Co-removal of hexavalent chromium through copper precipitation in synthetic wastewater. Environ. Sci. Technol. 37, 4281–4287.

Toby, B.H., 2001. EXPGUI, a graphical user interface for GSAS. J. Appl. Crystallogr. 34, 210–213, 2001.

Vhahangwele, M., Mugera, G.W., 2015. The potential of ball-milled South African bentonite clay for attenuation of heavy metals from acidic wastewaters: simultaneous sorption of Co^{2+}, Cu^{2+}, Ni^{2+}, Pb^{2+}, and Zn^{2+} ions. J. Environ. Chem. Eng. 3, 2416.

Wang, C., Zhou, J., Wang, Y., Yang, M., Li, Y., Meng, C., 2013. Synthesis of zeolite X from low-grade bauxite. J. Chem. Technol. Biotechnol. 88, 1350–1357.

Wruck, K., Millar, G.J., Wang, T., 2021. Transformation of heulandite type natural zeolites into synthetic zeolite LTA. Environ. Technol. Innov. 21, 101371.

Xie, W.M., Zhou, F.P., Bi, X.L., Chen, D.D., Li, J., Sun, S.Y., Liu, J.Y., Chen, X.Q., 2018. Accelerated crystallization of magnetic 4A-zeolite synthesized from red mud for application in removal of mixed heavy metal ions. Microporous Mesoporous Mater. 358, 441–449.

Yin, Y., Shen, C., Bi, X., Li, T., 2020. Removal of hexavalent chromium from aqueous solution by fabricating novel heteroaggregates of montmorillonite microparticles with nanoscale zero-valent iron. Sci. Rep. 10, 1–12.

Yoldi, M., Fuentes-Ordoñez, E.G., Korili, S.A., Gil, A., 2019. Zeolite synthesis from industrial wastes. Microporous Mesoporous Mater. 287, 183–191.

Yuna, Z., 2016. Review of the natural, modified, and synthetic zeolites for heavy metals removal from wastewater. Environ. Eng. Sci. 33, 443–454.

Zhang, Y., Zhou, L., Chen, L., Guo, Y., Guo, F., Wu, J., Dai, B., 2021. Synthesis of zeolite Na-P1 from coal fly ash produced by gasification and its application as adsorbent for removal of Cr(VI) from water. Front. Chem. Sci. Eng. 15, 518–527.